THE EUROPEAN
PHYSICAL JOURNAL A

Regular Article -Theoretical Physics

Finite-temperature equations of state of compact stars with hyperons: three-dimensional tables

Stefanos Tsiopelas[1] , **Armen Sedrakian**[1,2,a] , **Micaela Oertel**[3]

[1] Institute of Theoretical Physics, University of Wrocław, pl. M. Borna 9, 50-204 Wrocław, Poland
[2] Frankfurt Institute for Advanced Studies, 60438 Frankfurt am Main, Germany
[3] LUTH, Observatoire de Paris, Université PSL, CNRS, Université Paris Cité, 92190 Meudon, France

Abstract We construct tables of finite temperature equation of state (EoS) of hypernuclear matter in the range of densities, temperatures, and electron fractions that are needed for numerical simulations of supernovas, proto-neutron stars, and binary neutron star mergers and cast them in the format of COMPOSE database. The tables are extracted from a model that is based on covariant density functional (CDF) theory that includes the full $J^P = 1/2^+$ baryon octet in a manner that is consistent with the current astrophysical and nuclear constraints. We employ a parameterization with three different values of the slope of the symmetry energy $L_{\rm sym} = 30$, 50 and 70 MeV and fixed skewness $Q_{\rm sat} = 400$ MeV for above saturation matter. A model for the EoS of inhomogeneous matter is matched at sub-saturation density to the high-density hypernuclear EoS. We discuss the generic features of the resulting EoS and the composition of matter as a function of density, temperature, and electron fraction. The nuclear characteristics and strangeness fraction of these models are compared to the alternatives from the literature. The integral properties of static and rapidly rotating compact stars in the limit of zero temperature are discussed and confronted with the multimessenger astrophysical constraints.

1 Introduction

The equation of state (EoS) for dense, strongly interacting matter serves as the central input in an array of astrophysical simulations involving isolated compact objects and binary systems across various scenarios. The COMPOSE database [1,2] hosts a substantial collection of EoS data. Nevertheless, while numerous models exist to describe the composition of mature cold neutron stars, the range narrows considerably when considering the so-called general-purpose EoS, which encompass varying temperature, density, and electron fraction. Moreover, particularly for EoS models incorporating non-nucleonic degrees of freedom in dense and hot matter, like hyperons, recent years have imposed stringent astrophysical constraints, rendering several existing models incompatible with observations. It is expected that more constraints will emerge in the future in light of (multimessenger) observations of binary neutron star (BNS) mergers, isolated X-ray-emitting neutron stars in our proximity, and radio pulsars. In this context, the necessity of the inclusion of new EoS into this and other databases allows us to better cover and quantify the large uncertainties in the description of dense and hot strongly interacting matter. This paper describes the generation of general-purpose EoS tables in the temperature, density, and electron fraction space based on covariant density functional (CDF) models which include hyperonic degrees of freedom, for reviews see [3–5]. Specifically, CDFs for finite temperature hypernuclear matter of the kind that we will employ here have been constructed and applied to a range of astrophysical scenarios in the past [6–13].

Our general aim here is to cover the complete parameter space of temperature, density, and electron fraction, that is required by the simulations of the astrophysical scenarios mentioned above. We will employ recent new parametrizations of the CDF with density-dependent (DD) couplings [14] which allow for variations in the slope of the symmetry energy $L_{\rm sym}$ and the skewness $Q_{\rm sat}$. Here, we discuss the EoS with contributions from baryons, photons, and electrons/positrons to the EoS, the two latter components being treated as an ideal gas. The case of neutrino-trapped matter in the high-density range $n_B/n_{\rm sat} \geq 0.5$, where $n_{\rm sat}$ is the saturation density has been discussed in Refs. [11,12] where a different (DDME2) parameterization was used [15].

We will compare the results from this and other alternative parametrizations to the present results later on.

We further match the EoS of high-density (homogeneous) hypernuclear matter to that of low-density (inhomogeneous) nuclear matter. The low-density EoS corresponds to the one developed in Ref. [16] and is based on an improved nuclear statistical equilibrium among nucleons and nuclear clusters. Note that the hypernuclear matter is described within the class of CDF models which are consistent with the current astrophysical constraints on cold neutron star radii, tidal deformabilities, and maximum masses - models that emerged mostly after the 2010 detection of the 2-solar mass compact star, for a discussion see [5]. The model we employ includes the full baryon octet, i.e., strangeness 1 and 2 hyperons. It allows for σ^* and ϕ hidden strangeness mesons which mediate the hyperon-hyperon interaction.

Numerical simulations reveal that BNS mergers generate hot and dense strongly interacting matter during the post-merger stage [17–20]. The outcome of such a merger is contingent upon the combined masses of the merging objects and may lead to the formation of a black hole or a stable neutron star. In any scenario, a transient hot object is formed, and thus, the spectrum of gravitational waves emitted during this phase (potentially observable with advanced gravitational wave instruments, such as the Einstein Telescope [21]) carries distinctive characteristics reflecting the EoS of hot and dense matter. This EoS also governs the stability of the resulting object, influencing the course of its transient evolution [22], as well as the efficiency of dissipative processes [23–30], which should be incorporated into the commonly used ideal hydrodynamics simulations [31].

The emergence of hot and neutrino-rich compact objects is also anticipated through numerical simulations of core-collapse supernovas (CCSN). As the supernova progenitor contracts, a hot proto-neutron star is formed along with expanding ejecta [32–39]. The transient formation of dense, high-temperature matter occurs also when the progenitor possesses significant mass and the material collapses ultimately into a black hole [40–43].

The local characteristics of matter during the hot phase in the aforementioned astrophysical scenarios are primarily defined by factors such as density, temperature (or entropy), and the lepton fractions for electrons and muons. The EoS in this phase depends on multiple parameters, which can be compared to the more straightforward one-parameter EoS describing cold and β-equilibrated matter. Given the multitude of nuclear and astrophysical constraints imposed on the cold EoS we will briefly touch upon the predictions of underlying EoS for global properties of cold nucleonic and hypernuclear compact stars; such input is also required by the COMPOSE repository. Muons are excluded from our tables to maintain a three-dimensional representation of parameter space, focusing on temperature, density, and electron fraction.

This work is organized as follows. In Sect. 2 we review the high-density EoS of hypernuclear matter at finite temperatures, where Sect. 2.1 discusses the formalism, Sect. 2.2 – the choice of the coupling constants, Sect. 2.3 the conditions relevant for BNS mergers and CCSN and Sect. 2.4 the procedure of matching the low (inhomogeneous) and high-density (homogeneous) EoS. We present the numerical results on the EoS and composition in Sect. 3. The mass-radius (hereafter M-R) relation of static cold compact stars and the astrophysical constraints are discussed in Sect. 4. Section 5 is dedicated to the discussion of how our model compares to the alternative models. In Sect. 6 we provide a summary of our main results. We use the natural (Gaussian) units with $\hbar = c = k_B = 1$, and the metric signature $g^{\mu\nu} = \mathrm{diag}(1, -1, -1, -1)$.

2 Finite temperature equation of state of hypernuclear matter

The purpose of this section is to collect all the ingredients that are required for the construction of the three-dimensional tables. We review the physical model, the selection of the values for the couplings in the Lagrangian of the model, the thermodynamical conditions relevant for the cases of BNS and CCSN, and, finally, the matching to the low-density (subnuclear) EoS to the high-density one.

2.1 Formalism

The CDF model on which the finite-temperature EoSs is constructed is based on the Lagrangian

$$\mathscr{L} = \mathscr{L}_b + \mathscr{L}_m + \mathscr{L}_\lambda + \mathscr{L}_{\mathrm{em}}, \tag{1}$$

where the $J_B^P = \frac{1}{2}^+$ baryon Lagrangian is given by

$$\mathscr{L}_b = \sum_b \bar{\psi}_b \left[\gamma^\mu \left(i\partial_\mu - g_{\omega b}\omega_\mu - g_{\phi b}\phi_\mu - \frac{1}{2}g_{\rho b}\boldsymbol{\tau} \cdot \boldsymbol{\rho}_\mu \right) \right.$$
$$\left. - (m_b - g_{\sigma b}\sigma - g_{\sigma^* b}\sigma^*) \right] \psi_b, \tag{2}$$

with the index b summing over the $J_B^P = \frac{1}{2}^+$ baryon octet, which includes neutrons, protons, and Λ, $\Xi^{0,-}$, $\Sigma^{0,\pm}$ hyperons. The interaction is modeled via the non-strange sector mesons σ, ω_μ, and $\boldsymbol{\rho}_\mu$ which couple to all the members of the octet and hidden strangeness mesons σ^*, ϕ_μ, which couple only to hyperons. Here ψ_b are the Dirac fields of the baryon octet with masses m_b, g_{mb} are the meson–baryon couplings where m index runs over the different meson channels. Note that the meson states here do not correspond to

the ones in vacuum, but effectively describe the interaction of baryons taking into account multiple scattering and in-medium effects. It is assumed that the masses are close to those in vacuum, except the σ meson, which has a resonance structure and effectively represents two-pion state. Its mass is often used as a free parameter of a model. Their couplings to baryons, however, differ from the tree-level couplings in vacuum physics, i.e., are treated as fit parameters that account for the above-mentioned multiple scattering and in-medium effects.

The mesonic part of the Lagrangian is given by

$$\mathcal{L}_m = \frac{1}{2}\partial^\mu\sigma\,\partial_\mu\sigma - \frac{m_\sigma^2}{2}\sigma^2 - \frac{1}{4}\omega^{\mu\nu}\omega_{\mu\nu} + \frac{m_\omega^2}{2}\omega^\mu\omega_\mu$$
$$- \frac{1}{4}\boldsymbol{\rho}^{\mu\nu}\cdot\boldsymbol{\rho}_{\mu\nu} + \frac{m_\rho^2}{2}\boldsymbol{\rho}^\mu\cdot\boldsymbol{\rho}_\mu + \frac{1}{2}\partial^\mu\sigma^*\partial_\mu\sigma^* - \frac{m_\sigma^{*2}}{2}\sigma^{*2}$$
$$- \frac{1}{4}\phi^{\mu\nu}\phi_{\mu\nu} + \frac{m_\phi^2}{2}\phi^\mu\phi_\mu,$$
(3)

where m_σ, m_{σ^*}, m_ω, m_ϕ and m_ρ denote the meson masses. The field-strength tensors for vector fields are given by

$$\omega_{\mu\nu} = \partial_\mu\omega_\nu - \partial_\mu\omega_\nu,$$
(4)
$$\phi_{\mu\nu} = \partial_\mu\phi_\nu - \partial_\mu\phi_\nu,$$
(5)
$$\boldsymbol{\rho}_{\mu\nu} = \partial_\nu\boldsymbol{\rho}_\mu - \partial_\mu\boldsymbol{\rho}_\nu.$$
(6)

As mentioned above, charged leptons are treated as an ideal gas, thus the Lagrangian is given by the free Dirac Lagrangian

$$\mathcal{L}_\lambda = \sum_\lambda \bar{\psi}_\lambda(i\gamma^\mu\partial_\mu - m_\lambda)\psi_\lambda,$$
(7)

where ψ_λ are leptonic fields and m_λ are their masses.

The general-purpose tables of EoS commonly include only electrons and positrons and neglect the contributions from other leptons. Charged τ-leptons are too massive to appear in stellar matter. Including charged muons treated as an ideal gas in an EoS table is a priori straightforward since the main difficulty resides in determining the EoS for the strongly interacting baryons. Since in addition only a few simulations up to now evolve a muon fraction, see e.g. [44], we refrain here from adding a fourth dimension to our already rather memory-consuming tables. A similar reasoning applies to the contributions of neutrinos which in the trapped regime contribute to energy density and pressure. These contributions can be cast into analytical expressions which can easily be added if needed. Note that in the case when strong electromagnetic fields are present (1) should include the electromagnetic contribution $\mathcal{L}_{em}$ which we neglect here. Examples, where such term is important are the cores of magnetars that may support magnetic fields of the order of 10^{18} G [45–47] as well as magnetar crusts

where the physics of finite nuclei may be affected by magnetic fields [48–51]. Electromagnetic part of the Largangian contributes also to the Coulomb corrections in inhomogeneous matter, see e.g. Ref. [16], but these are not relevant for present discussion. For the Lagrangian given by Eq. (1) the evaluation of the pressure and energy density of the constituents can be added with $\lambda = e$

$$P = P_b + P_m + P_e + P_r,$$
(8)
$$\mathcal{E} = \mathcal{E}_b + \mathcal{E}_m + \mathcal{E}_e,$$
(9)

where the contributions due to mesons and $J_B^P = \frac{1}{2}^+$-baryons are given by

$$P_m = -\frac{m_\sigma^2}{2}\sigma^2 - \frac{m_\sigma^{*2}}{2}\sigma^{*2} + \frac{m_\omega^2}{2}\omega_0^2 + \frac{m_\phi^2}{2}\phi_0^2 + \frac{m_\rho^2}{2}\rho_{03}^2,$$
(10)

$$\mathcal{E}_m = \frac{m_\sigma^2}{2}\sigma^2 + \frac{m_\sigma^{*2}}{2}\sigma^{*2} + \frac{m_\omega^2}{2}\omega_0^2 + \frac{m_\phi^2}{2}\phi_0^2 + \frac{m_\rho^2}{2}\rho_{03}^2,$$
(11)

$$P_b = \sum_b \frac{g_b}{6\pi^2}\int_0^\infty \frac{dk\,k^4}{E_k^b}\left[f(E_k^b - \mu_b^*) + f(E_k^b + \mu_b^*)\right],$$
(12)

$$\mathcal{E}_b = \sum_b \frac{g_b}{2\pi^2}\int_0^\infty dk\,k^2 E_k^b\left[f(E_k^b - \mu_b^*) + f(E_k^b + \mu_b^*)\right],$$
(13)

where $f(E) = [1 + \exp(E/T)]^{-1}$ is the Fermi distribution function at temperature T, the single-particle energies of baryons are given by $E_k^b = \sqrt{k^2 + m_b^{*2}}$, $g_b = 2J_b + 1 = 2$ is the spin ($J_b = 1/2$) degeneracy factor of the baryon octet, and the effective masses are defined as

$$m_b^* = m_b - g_{\sigma b}\sigma - g_{\sigma^* b}\sigma^*.$$
(14)

The effective chemical potentials are given by

$$\mu_b^* = \mu_b - g_{\omega b}\omega_0 - g_{\phi b}\phi_0 - g_{\rho b}\rho_{03}I_{3b} - \Sigma^r,$$
(15)

where the so-called rearrangement term is given by

$$\Sigma^r = \sum_{b,d}\left(\frac{\partial g_{\omega b}}{\partial n_b}\omega_0 n_b + \frac{\partial g_{\rho b}}{\partial n_b}I_{3b}\rho_{03}n_b + \frac{\partial g_{\phi b}}{\partial n_b}\phi_0 n_b\right.$$
$$\left. - \frac{\partial g_{\sigma b}}{\partial n_b}\sigma n_b^s - \frac{\partial g_{\sigma^* b}}{\partial n_b}\sigma^* n_b^s\right)$$
(16)

and the pressure contribution from this term is $P_r = n_B\Sigma_r$. Note that we implicitly used the fact that the baryon-meson couplings depend on the vector density, therefore the rearrangement term appears in Eq. (15) for the chemical potentials. If, however, scalar-density dependence is used, as in the MPE model of Ref. [52], then the formalism needs some modifications [14]. The mesonic fields in Eqs. (10), (11) and the following equations correspond to the mean-field values.

Their expectation values in the infinite system approximations are standard and we will not write them down here. The system of equations for baryons is closed by the expressions for the scalar and baryon (vector) number densities:

$$n_b = \frac{g_b}{2\pi^2} \int_0^\infty k^2 dk \left[f(E_k^b - \mu_b^*) - f(E_k^b + \mu_b^*) \right], \quad (17)$$

$$n_b^s = \frac{g_b}{2\pi^2} \int_0^\infty \frac{k^2 dk \, m_b^*}{E_k^b} \left[f(E_k^b - \mu_b^*) + f(E_k^b + \mu_b^*) \right]. \quad (18)$$

The electronic contribution is given by

$$P_e = \frac{g_e}{6\pi^2} \int_0^\infty \frac{dk \, k^4}{E_k^e} \left[f(E_k^e - \mu_e) + f(E_k^e + \mu_e) \right], \quad (19)$$

$$\mathcal{E}_e = \frac{g_e}{2\pi^2} \int_0^\infty dk \, k^2 E_k^e \left[f(E_k^e - \mu_e) + f(E_k^e + \mu_e) \right], \quad (20)$$

where the degeneracy factor for electrons $g_e = 2$. Electronic energies are given just by their kinetic energy $E_k^e = \sqrt{k^2 + m_e^2}$, where m_e is given by the free mass of an electron.

2.2 Coupling constants

In total six tables were constructed, three of which are purely nucleonic and are based on the parameterization of Ref. [14]. The other three EoS contain in addition hyperons. The three nucleonic EoS differ by the value of the slope of the symmetry energy $L_{sym} = 30$, 50 and 70 MeV and have fixed skewness Q_{sat}; we will abbreviate them as DDLS(30), DDLS(50), and DDLS(70), respectively. The value $Q_{sat} = 400$ MeV was chosen to ensure that the maximum masses of hypernuclear stars surpass the lower bound of two solar masses. The considered range for $30 \leq L_{sym} \leq 70$ MeV accommodates existing uncertainties associated with neutron skin measurements and neutron star radii [53]. Consequently, our ensemble of EoS facilitates investigations of the impact of varying the symmetry energy slope on dynamic phenomena such as supernova explosions and BNS mergers.

Let us now recall that the energy density of nuclear matter in the vicinity of saturation density and isospin-symmetrical limit can be expressed via a double-expansion in the Taylor series:

$$E(\chi, \delta) \simeq E_{sat} + \frac{1}{2!} K_{sat} \chi^2 + \frac{1}{3!} Q_{sat} \chi^3$$
$$+ \left(J_{sym} + L_{sym} \chi + \frac{1}{2!} K_{sym} \chi^2 \right.$$
$$\left. + \frac{1}{3!} Q_{sym} \chi^3 \right) \delta^2 \quad (21)$$

Table 1 The ratios of the couplings of hyperons to mesons to those of nucleons at saturation density, i.e., $n_0 = n_{sat}$

$b\backslash R$	$R_{\omega b}$	$R_{\phi b}$	$R_{\rho b}$	$R_{\sigma b}$	$R_{\sigma^* b}$
Λ	2/3	$-\sqrt{2}/3$	0	0.6106	0.4777
Σ	2/3	$-\sqrt{2}/3$	2	0.4426	0.4777
Ξ	1/3	$-2\sqrt{2}/3$	1	0.3024	0.9554

where $\chi = (n - n_{sat})/3n_{sat}$ and $\delta = (n_n - n_p)/n$, with n_n and n_p being the neutron and proton densities.

The definition of the coefficients of the expansion are standard and are given, e.g., in Ref. [5]. For the density dependence of the nucleon-meson couplings, we assume a standard form [54]

$$g_{iN}(n_B) = g_{iN}(n_0) h_i(x), \quad (22)$$

where $x = n_B/n_0$ and n_0 is a reference density specified in the parametrization.

$$h_i(x) = a_i \frac{1 + b_i(x + d_i)^2}{1 + c_i(x + d_i)^2}, \quad i = \sigma, \omega, \quad (23)$$

$$h_\rho(x) = e^{-a_\rho(x-1)}. \quad (24)$$

The explicit values of couplings and parameters determining the density-dependence are given in Ref. [14]. To complete the discussion, let us note that the saturation density $n_{sat} = 0.152$ fm^{-3}, the binding energy per particle in symmetrical nuclear matter at saturation density $E_B = -16.14$ MeV, the compressibility $K = 251$ MeV and effective nucleon mass $m_{n,p}^*/m_N = 0.57$ MeV (where $m_N = 939$ MeV is the bare mass) for the DDLS models are by construction the same as for the DDME2 model. The symmetry energy E_{sym}, however, changes with the value of the L_{sym}, specifically, $E_{sym} = 30.1, 32.2, 34.0$ MeV for $L_{sym} = 30$, 50 and 70 MeV, respectively.

The density dependence of the couplings for hyperons is the same as those for nucleonic ones, but their strengths at the reference density n_0 are different. The ratios of the hyperonic to nucleonic ones are given in Table 1. The depths of hyperonic potentials in the symmetric nuclear matter are $U_\Lambda(n_{sat}) = -30$ MeV $U_\Xi(n_{sat}) = -14$ MeV and $U_\Sigma(n_{sat}) = +30$ MeV.

2.3 Adapting CDF to conditions in CCSN and BNS merger remnants

For zero-temperature computations, we will assume weak-equilibrium among the members of the baryon octet and electrons. It is assumed that neutrinos freely escape the star and, therefore, do not form a statistical ensemble. This implies the
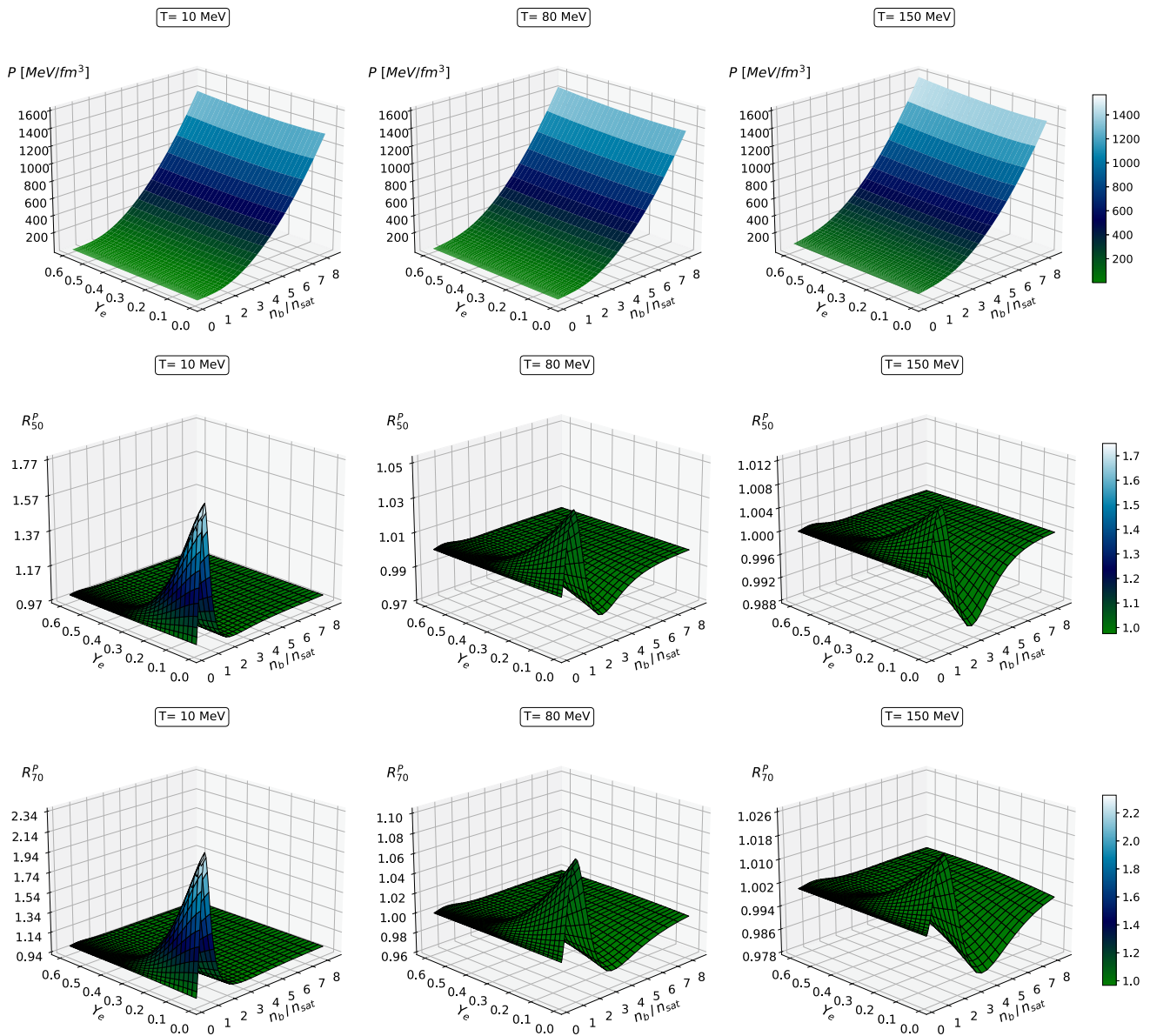
Fig. 1 Upper panel: pressure of nucleonic matter as a function of baryon density (normalized by the saturation density n_{sat}) and electron fraction for $L_{sym} = 30$ MeV and temperatures $T = 10$ MeV (left), $T = 80$ MeV (middle) and $T = 150$ MeV (right). Middle panel: ratio of the pressure of nucleonic matter with $L_{sym} = 50$ MeV to the pres-sure of nucleonic matter with $L_{sym} = 30$ MeV as a function of baryon density (normalized by the saturation density n_{sat}) and electron frac-tion for temperatures $T = 10$ MeV (left), $T = 80$ MeV (middle) and $T = 150$ MeV (right). Lower panel: same as the middle panel but for the ratio of pressure at $L_{sym} = 70$ MeV to that at $L_{sym} = 30$ MeV

following relations among the chemical potentials

$$\mu_\Lambda = \mu_{\Sigma^0} = \mu_{\Xi^0} = \mu_n = \mu_B, \tag{25}$$

$$\mu_{\Sigma^-} = \mu_{\Xi^-} = \mu_B - \mu_Q, \tag{26}$$

$$\mu_{\Sigma^+} = \mu_B + \mu_Q, \tag{27}$$

where μ_B and $\mu_Q = \mu_p - \mu_n = -\mu_e$ are the baryon and charge chemical potentials. An additional constraint is imposed by the charge neutrality condition

$$n_p + n_{\Sigma^+} - n_{\Sigma^-} + n_{\Xi^-} - n_{e^-} + n_{e^+} = 0. \tag{28}$$

where $e^\pm$ refers to electrons and positrons, respectively. We will work below with a fixed electron fraction which is given by $Y_e = (n_{e^-} - n_{e^+})/n_B$.

2.4 Matching to low-density matter for the general-purpose tables

In numerical simulations of CCSN or BNS mergers, in gen-eral, the EoS is incorporated in the form of tables covering the necessary ranges in thermodynamic parameters. The latter
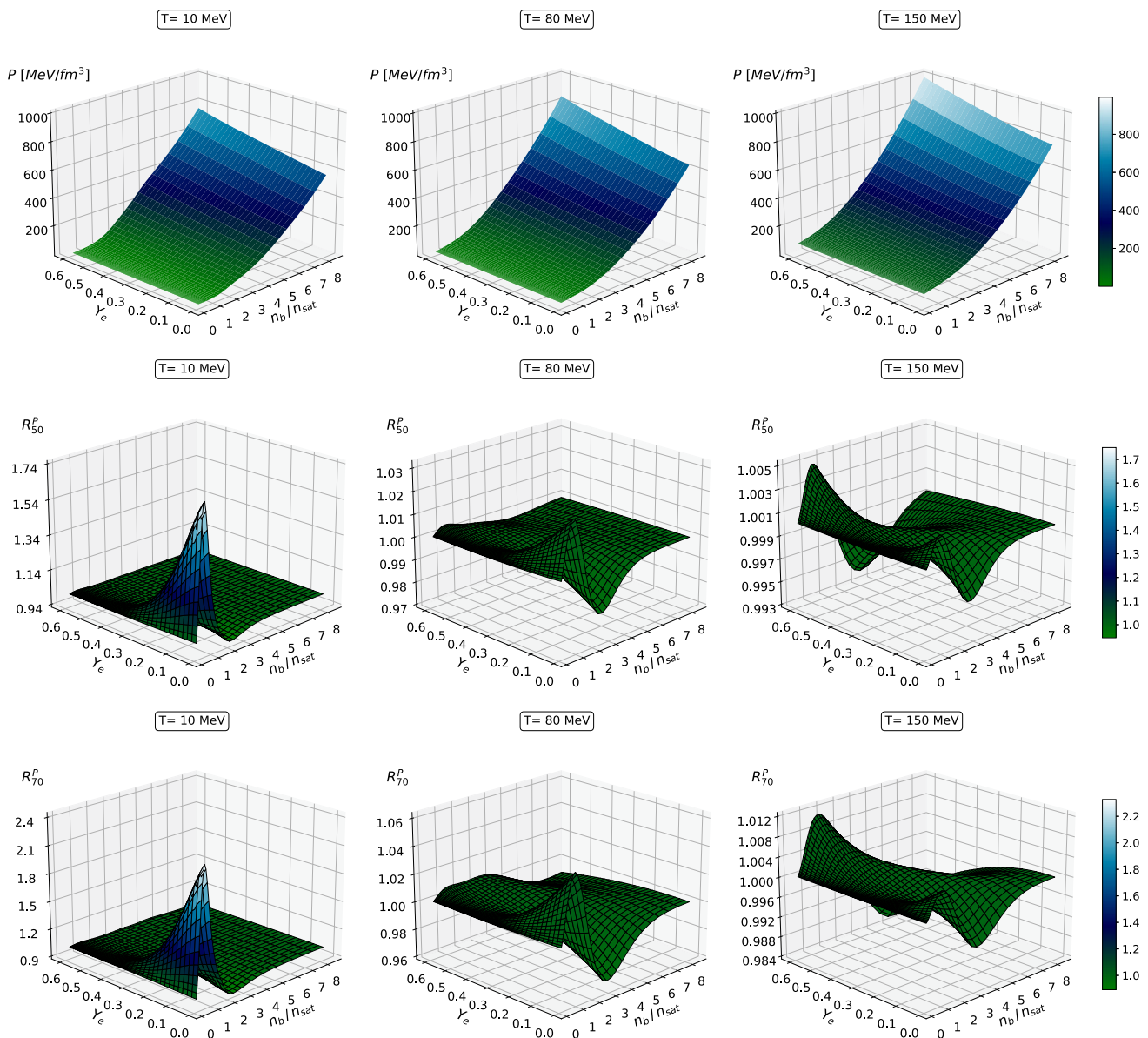
Fig. 2 Upper panel: pressure of hypernuclear matter as a function of baryon density (normalized by the saturation density n_{sat}) and electron fraction for $L_{sym} = 30$ MeV and temperatures $T = 10$ MeV (left), $T = 80$ MeV (middle) and $T = 150$ MeV (right). Middle panel: ratio of the pressure of hypernuclear matter with $L_{sym} = 50$ MeV to the pressure of hypernuclear matter with $L_{sym} = 30$ MeV as a function of baryon density (normalized by the saturation density n_{sat}) and electron fraction for temperatures $T = 10$ MeV (left), $T = 80$ MeV (middle) and $T = 150$ MeV (right). Lower panel: same as the middle panel but for the ratio of pressure at $L_{sym} = 70$ MeV to that at $L_{sym} = 30$ MeV

are mostly chosen to be temperature, baryon number density, and electron fraction (as mentioned above, muon fraction needs an additional evolution equation and is in general not included) with values typically in between $0.1 \lesssim T \lesssim 100$ MeV, $10^{-12} \lesssim n_B \lesssim 1$ fm^{-3}, and $0.01 \lesssim Y_e \lesssim 0.6$ [3] to describe matter under the very different thermodynamic conditions occurring during the CCSN or the BNS merger. The models presented here only consider homogeneous matter, i.e. they are not adapted to the low-density and temperature region where nuclear clusters coexist with unbound nucle-

ons. To extend our models into that region and produce a complete general-purpose table, we have chosen to match the high-density EoS to the low-density HS(DD2) one [16] at a density of $n_B = 0.04$ fm^{-3}. If for the given values of T and Y_e, matter is not homogeneous in the original HS(DD2) table at this density, then the matching is performed at the lowest density for homogeneous matter. The HS(DD2) model describes inhomogeneous matter within an extended nuclear statistical equilibrium approach [16], treating the interaction of unbound nucleons within the DD2 [55] model. At low
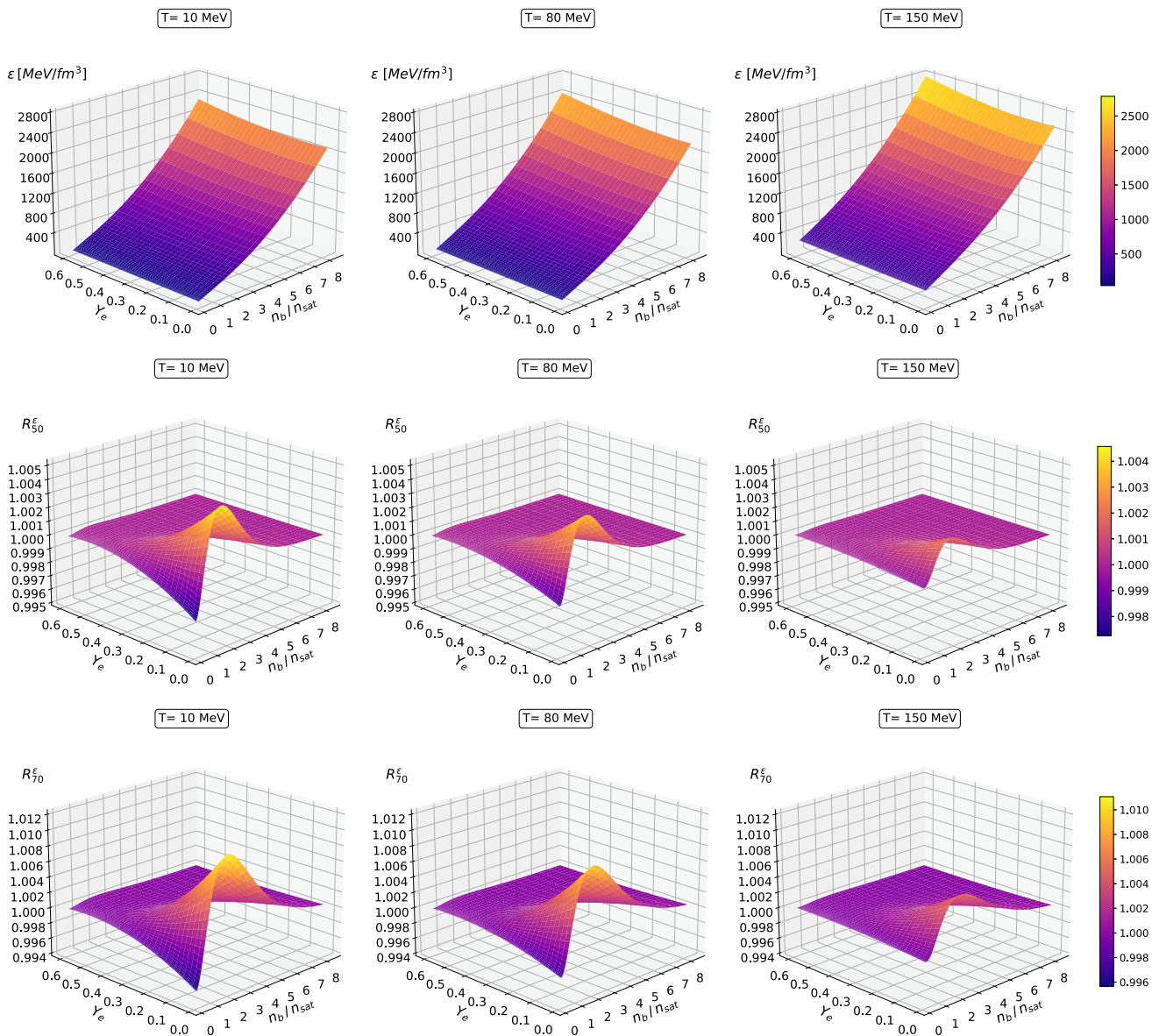
Fig. 3 Upper panel: energy density of nucleonic matter as a function of baryon density (normalized by the saturation density n_{sat}) and electron fraction for $L_{sym} = 30$ MeV and temperatures $T = 10$ MeV (left), $T = 80$ MeV (middle) and $T = 150$ MeV (right). Middle panel: ratio of the energy density of nucleonic matter with $L_{sym} = 50$ MeV to energy density of nucleonic matter with $L_{sym} = 30$ MeV as a func-

tion of baryon density (normalized by the saturation density n_{sat}) and electron fraction for temperatures $T = 10$ MeV (left), $T = 80$ MeV (middle) and $T = 150$ MeV (right). Lower panel: same as the middle panel but for the ratio of energy density at $L_{sym} = 70$ MeV to that at $L_{sym} = 30$ MeV

densities, the DD2 interaction is very close to the models employed here and at the densities at which we perform the matching, only nucleons should be present. This ensures a smooth matching of inhomogeneous to homogeneous matter upon constructing our general-purpose table. The only weakness is that we miss a fraction of hyperons and Δ-resonances at high temperatures and low densities. Indeed in this regime, the hyperon fractions are substantial, see Figs. 5 and 6 and Refs. [3,5,8,9,12] and matching the purely nuclear HS(DD2) EoS within our tables induces small discontinuities in partic-

ular in the hyperon fractions. Their influence on thermodynamic quantities is small. We will improve on this point in a future version of the tables.

3 Equation of state and composition of hypernuclear matter

Our tables were generated through self-consistent solutions of the equations for the meson fields (in the static approxi-
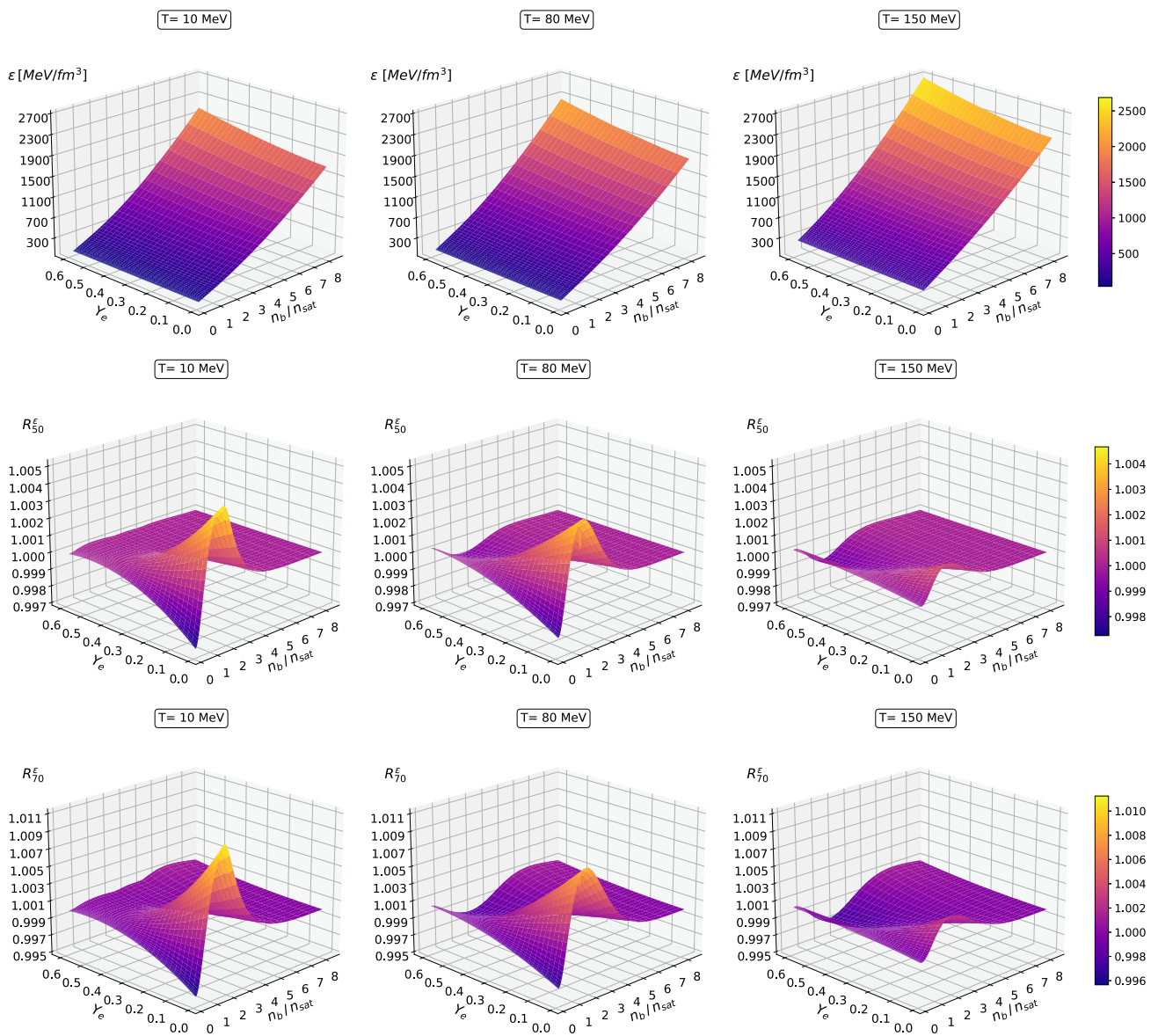
Fig. 4 Upper panel: energy density of hypernuclear matter as a function of baryon density (normalized by the saturation density n_{sat}) and electron fraction for $L_{\text{sym}} = 30$ MeV and temperatures $T = 10$ MeV (left), $T = 80$ MeV (middle) and $T = 150$ MeV (right). Middle panel: ratio of the energy density of hypernuclear matter with $L_{\text{sym}} = 50$ MeV to the energy density of hypernuclear matter with $L_{\text{sym}} = 30$ MeV as a function of baryon density (normalized by the saturation density n_{sat}) and electron fraction for temperatures $T = 10$ MeV (left), $T = 80$ MeV (middle) and $T = 150$ MeV (right). Lower panel: same as the middle panel but for the ratio of energy density at $L_{\text{sym}} = 70$ MeV to that at $L_{\text{sym}} = 30$ MeV

mation) and the scalar and baryon densities (17) and (18) for fixed values of temperature, density, and electron fraction. The neutrino contribution is typically added within the simulations from the employed neutrino treatment which also accounts consistently for neutrino trapping, which happens typically in dense matter above a temperature of several MeV. Muons are neglected likewise to limit the dimensionality of the table to three.

We next illustrate the content of the tables by showing selected results, which are obtained through cuts in three-dimensional space spanned by density, temperature, and electron fraction. The finite-temperature pressure as a function of density and electron fraction for nucleonic matter is shown in Fig. 1 for $L_{\text{sym}} = 30$ MeV and three values of fixed temperature. We show in the same figure the ratios of pressures $P[L_{\text{sym}} = 50 \text{ MeV}]/P[L_{\text{sym}} = 30 \text{ MeV}]$ and $P[L_{\text{sym}} = 70 \text{ MeV}]/P[L_{\text{sym}} = 30 \text{ MeV}]$ to visualize the
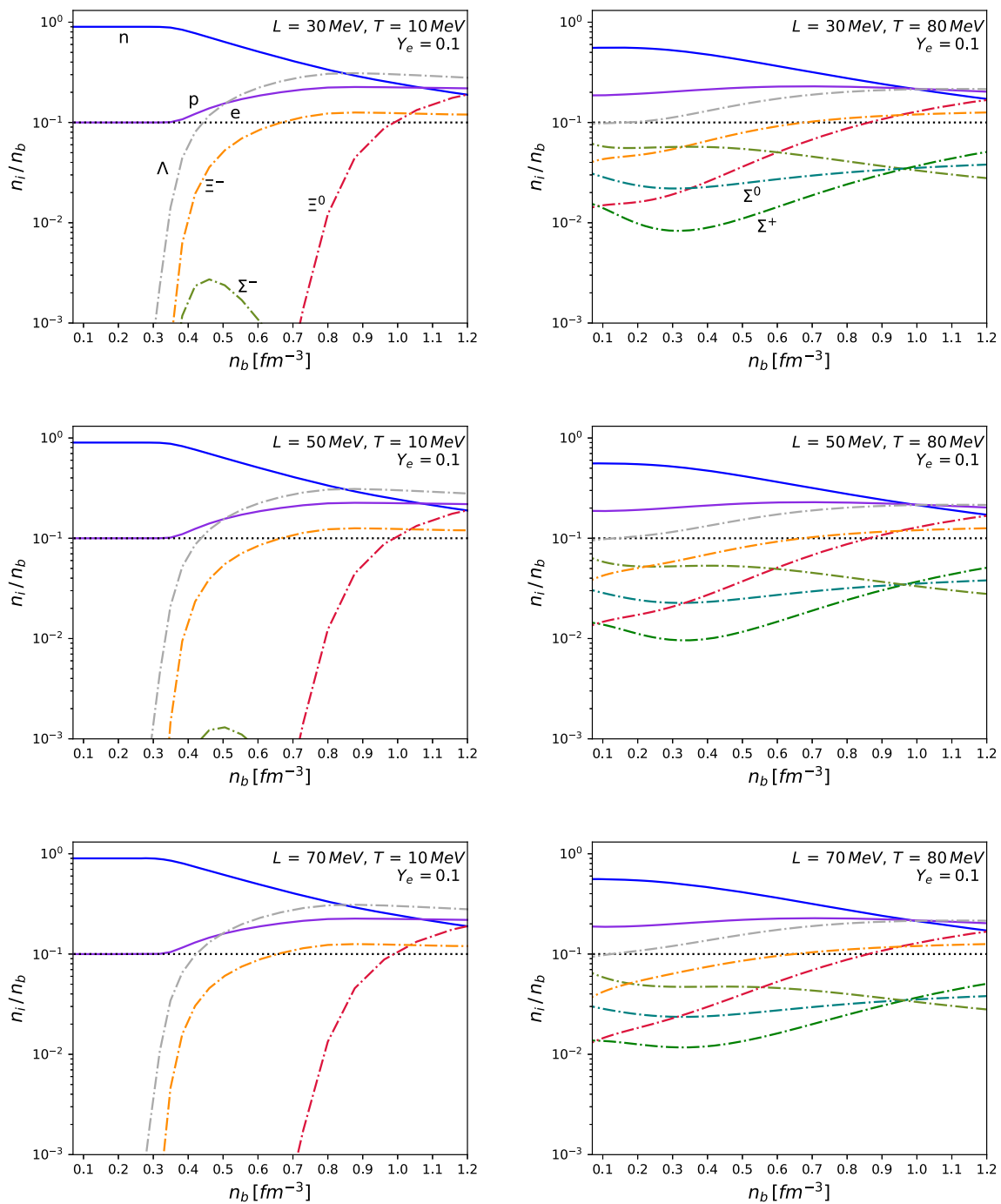
Fig. 5 Composition of matter for the three different values of L at a constant electron fraction of $Y_e = 0.1$ and temperature of $T = 10$ MeV (left panels) and $T = 80$ MeV (right panels). All figures correspond to the hypernuclear EoS

changes with the change in the symmetry energy slope L_{sym}. As expected, pressure is an increasing function of density; The ratios of pressure for different L_{sym} values tend to unity in the limit of large densities where pressure is dominated by the value of Q_{sat} and the influence of L_{sym} is negligible. The ratios increase as one moves away from the symmetric limit. It is also obvious that the ratios are numerically larger the

larger the difference in L_{sym}. Increasing the temperature for a fixed value of L_{sym} diminishes the ratios of the pressures as they are increasingly dominated by thermal effects rather than interactions.

Figure 2 shows the EoS for the same parameters as in Fig. 1, but in the presence of hyperons. It is seen that this new feature strongly softens the EoS due to the onset of the
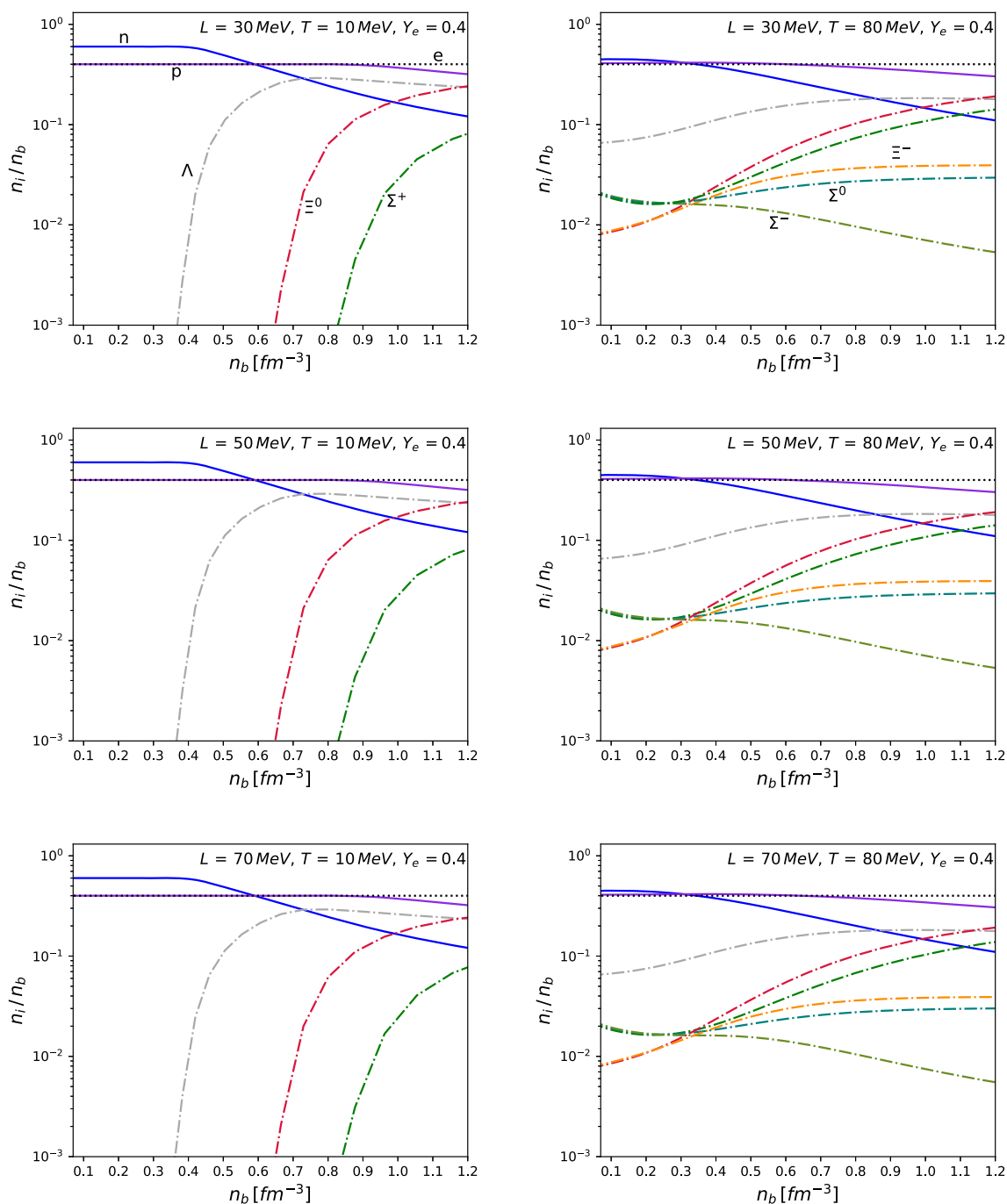
Fig. 6 Same as in Fig. 5, but for an electron fraction of $Y_e = 0.4$

new degrees of freedom, which allow for the reduction of the degeneracy pressure of nucleons. The ratios of the pressures at various L_{sym} show the same trends seen in the nucleonic case since the factors that determine them are unchanged when hyperons are added.

Figure 3 shows the energy density of nucleonic matter as a function of density and electron fraction for $L_{sym} = 30$ MeV and again the same three values of fixed

temperature. It also shows the ratios of energy densities $\mathcal{E}[L_{sym} = 50\text{ MeV}]/\mathcal{E}[L_{sym} = 30\text{ MeV}]$ and $\mathcal{E}[L_{sym} = 70\text{ MeV}]/\mathcal{E}[L_{sym} = 30\text{ MeV}]$. The general features that we already discussed in the case of pressure are repeated in the case of energy density as well. (a) It is an increasing function of density and has a minimum at the isospin symmetric limit. (b) The ratios of energy densities for different L_{sym} values are peaked at $Y_e \to 0$ (pure neutron matter) as the
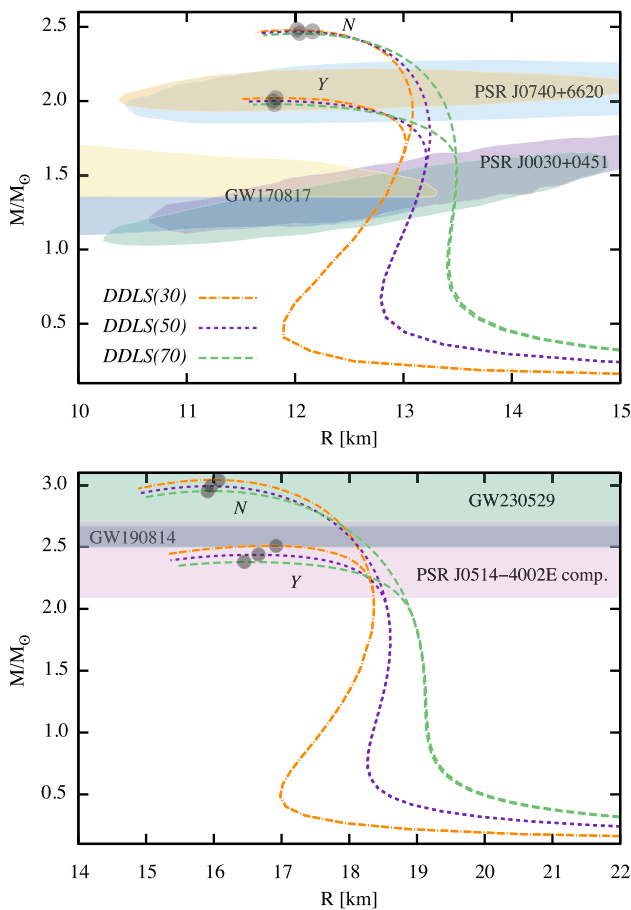
Fig. 7 Gravitational mass versus radius for non-rotating (upper panel) and maximally fast rotating (lower panel) stars. In the case of rotating stars, R refers to the equatorial radius. The upper three branches, labeled as N, correspond to nucleonic, and the lower three labeled as Y – to hyperonic stars for EoS models DDLS(30), DDLS(50) and DDLS(70) for fixed value of $Q_{sat} = 400$ MeV. The ellipses in the upper panel show 90% CI regions for PSR J0030+0451 [57,58], PSR J0740+6620 [59, 60] and gravitational wave event GW170817 [61]. The colored regions correspond to the light member in the GW190814 event (blue) [62], the heavy member in the GW230529 event (light green) [63], and the heavy companion of PSR J0514-4002E (violet) [64]. The dots indicate the location of the maximum mass for any given sequence, see also Table 2

asymmetry energy is maximal in this limit. (c) Again, as in the case of pressure ratios, the ratios of energy densities are numerically larger the larger the difference in L_{sym}.

Figure 4 shows the same quantities as in Fig. 3 but for hypernuclear matter. The energy density ratios at different L_{sym} values exhibit the same trends already observed in the nucleonic case, and we do not repeat the discussion here.

3.1 Composition of matter

We next turn to the composition of matter under the conditions considered in this work. Figure 5 shows the composition of finite-temperature hyperonic matter at two temperatures

$T = 10$ and 80 MeV for three values of $L_{sym} = 30, 50$ and 70 MeV and fixed $Y_e = 0.1$. At $T = 10$ MeV hyperons Λ, Ξ^-, Σ^- and Ξ^0 appear in the given order with increasing density, with the Σ^- hyperon fraction being strongly suppressed by the highly repulsive potential in nuclear matter at saturation density. Since the chemical potentials are still much larger than the temperature, this arrangement is qualitatively the same as the one at zero temperature and shows also relatively sharp thresholds for the appearance of hyperons. The large negative charge chemical potential in matter with low electron fractions favors here the negatively charged hyperons over their isospin partners, see e.g. the discussion in [56]. For higher temperature $T = 80$ MeV the thresholds disappear and hyperon abundances extend deep in the low-density regime. The isospin triplet of $\Sigma^{\pm,0}$ is now thermally supported with amounts comparable to other hyperons. As pointed out in Refs. [11,12] there is a special isospin degeneracy point where the fractions within each isospin multiplet coincide. This is visible for Σ and Ξ hyperons at $T = 80$ MeV. At this degeneracy point, there is a reversal in the dominance of the abundances of the hyperons present. For example, as density increases, the Σ^- hyperon goes over from being the most abundant to the least abundant hyperon in the Σ-hyperon multiplet. Similar behavior is seen as well for Ξ^- and Ξ^0 fractions. The mechanism underlying the isospin degeneracy point is discussed in Ref. [12], where it is pointed out that this effect is related to the vanishing of the charge chemical potential at that point. The variations of the abundances of hyperons with the value of L_{sym} are large quantitatively, see however the visible suppression of Σ^- hyperons with increasing L_{sym}.

Figure 6 shows the same for an electron fraction of $Y_e = 0.4$. The higher charge chemical potential in this less neutron-rich regime leads to a different composition where the negatively charged particles within an isospin multiplet are no longer favored. This can be seen at $T = 10$ MeV with the Ξ^0 and the Σ^+ appearing first and at $T = 80$ MeV, the isospin degeneracy point is shifted to lower baryon number densities. The value of L_{sym} only has a minor influence on the results because the contribution of the symmetry energy is small for nearly symmetrical matter.

4 Cold equation of state and astrophysical constraints

While the finite-temperature EoS is needed for transient astrophysical scenarios involving neutron stars, the cold (zero-temperature) limit of the EoS is sufficient to describe their secular time scale evolution independent of their observational manifestations as pulsars, accreting X-ray neutron stars, etc. Currently, available astrophysical constraints on the global parameters of neutron stars put limits on the cold β-equilibrated EoS, therefore we complete the discussion

Table 2 The upper half of the table refers to the properties of non-rotating spherically symmetric cold β-equilibrated, neutrino-transparent, compact stars based on the EoS models considered in this work. The first three columns show the maximum gravitational mass ($M_{G,\max}$), the corresponding radius ($R_{\max}$) and central energy density ($\varepsilon_{B,\max}$) for the (cold) EoS with nucleons only (N) and hyperons (Y). The remaining column shows the radius at $M_G = 1.4 M_\odot$ mass. The lower half shows the same quantities for maximally rotating (Keplerian) sequences. The listed radii correspond to equatorial ones in this case. In addition, we show the Keplerian frequency $\Omega_{\max}^K$ for maximum mass nucleonic and hyperonic stars. The same values for a $1.4 M_\odot$ stars, which coincide in the cases of nucleonic and hyperonic stars, are given by $\Omega_{1.4M_\odot}^K/(10^4\,\text{Hz}) = 0.57,\ 0.54,\ 0.52$ for DDLS(30), DDLS(50) and DDLS(70) models

Model	$M_{G,\max}$ $(M_\odot)$	$R_{\max}$ (km)	$\varepsilon_{B,\max}$ $(10^{15}\,\text{g cm}^{-3})$	$R_{1.4M_\odot}$ (km)	$\Omega_{\max}^K/10^4$ (Hz)
N, DDLS(30)	2.48	12.02	1.85	12.87	–
N, DDLS(50)	2.47	12.16	1.90	13.15	–
N, DDLS(70)	2.46	12.04	1.85	13.47	–
Y, DDLS(30)	2.02	11.82	1.94	12.87	–
Y, DDLS(50)	2.00	11.80	2.02	13.15	–
Y, DDLS(70)	1.98	11.81	2.08	13.48	–
N, DDLS(30)	3.04	16.07	1.53	18.06	0.96
N, DDLS(50)	2.99	15.96	1.60	18.53	0.97
N, DDLS(70)	2.95	15.91	1.67	19.10	0.97
Y, DDLS(30)	2.51	16.92	1.40	18.06	0.82
Y, DDLS(50)	2.44	16.66	1.53	18.53	0.83
Y, DDLS(70)	2.38	16.45	1.68	19.10	0.83

of the finite-temperature EoS by confronting its zero temperature limit with the observations, see also Ref. [14]. In Fig. 7 the 90% CI ellipses show three key constraints involving PSR J0030+0451 [57,58], PSR J0740+6620 [59,60], and the gravitational wave event GW170817 [61]. The first two objects are pulsars with constrained radii. PSR J0030+0451 has a gravitational mass $M = 1.34^{+0.15}_{-0.16}M_\odot$ and radius $R = 12.71^{+1.14}_{-1.19}$ km (68% CI) [57]. An alternative evaluation leads to $M = 1.44^{+0.15}_{-0.14}M_\odot$ and $R = 13.02^{+1.24}_{-1.06}$ km (68% CI) [58]. For the more massive compact star PSR J0740+6620 one finds the mass $2.08 \pm 0.07 M_\odot$ and radius $13.7^{+2.6}_{-1.5}$ km [60] or, alternatively, $2.072^{+0.067}_{-0.066}M_\odot$ and $12.39^{+1.30}_{-0.98}$ km (68% CI) [59].

The static solutions of Einstein's equations in spherical symmetry were obtained by solving the Tolman–Oppenheimer–Volkoff equations [65] for cold β-equilibrated EoS models DDLS(30), DDLS(50) and DDLS(70) for purely nucleonic matter (labeled as N) and hypernuclear matter (labeled as Y), see Fig. 7. In addition, the same figure shows the M-R relations for maximal fast rotating (Keplerian) sequences for rigid rotation for the same EoSs. These were computed with the RNS code [66]. Table 2 lists the maximal gravitational mass $M_{G,\max}$ of each sequence considered, as well as the corresponding radius ($R_{\max}$), and central density ($\varepsilon_{B,\max}$). The well-known softening of the EoS once hyperons are allowed results in the lower maximum masses of non-rotating and rapidly rotating stars, see Fig. 7 and Table 2. The masses and radii of the non-rotating sequences are compatible with the NICER inferences for canonical (i.e.

$M \sim 1.4 M_\odot$) and massive (i.e. $M \sim 2 M_\odot$) compact stars. It is evident that the N and Y sequences differ only when the central density of a configuration is above the threshold for the onset of hyperons. The M-R tracks are fully consistent with GW170817 ellipses for DDLS(30) and DDLS(50) models but require a smaller radius than predicted by the DDLS(70) model. We still keep this model in our collection as we aim to cover a broad range of L_{sym} values. Note that CDF models that allow for Δ resonances in addition to hyperons can produce smaller radii for intermediate-mass stars without affecting the maximum mass of a sequence, see Refs. [10,67–71].

The lower panel of Fig. 7 shows the mass-radius diagram for maximally fast rotating nucleonic and hyperonic stars, where the radius is the equatorial one. Table 2 lists the key parameters of maximally fast rotating stars - the gravitational mass, equatorial radius, and Keplerian frequency for the maximum mass star. The interest in rotating hypernuclear (and Δ-admixed) compact stars arose in connection with the possibility that the light companion in the highly asymmetric binary compact object coalescence event GW190814 [62] with estimated mass in the range $2.5 \leq M/M_\odot \leq 2.67$ is a rotating hypernuclear star. The range of inferred masses is within the "mass gap" where neither neutron stars nor black holes were found and are also hard to form with current theoretical models. This scenario has been explored with the DDME2 parametrization with some variations of the hyperonic coupling constants [72–75]. Reference [75] finds hypernuclear stars with masses close to $2.5 M_\odot$ can be achieved
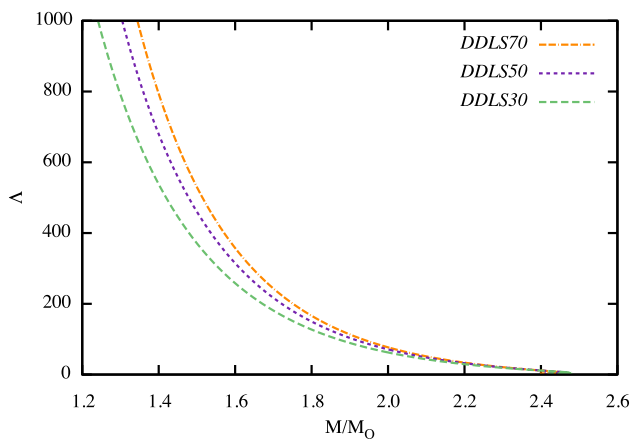
Fig. 8 Tidal deformability Λ of nucleonic models DDLS30, DDLS50, and DDLS70. Current constraint, inferred from GW170817 event, sets an upper limit on tidal deformability for an $1.4M_\odot$ mass star $\Lambda_{1.4} < 800$. Data taken from Ref. [14]

in the case of maximally fast (Keplerian) rotation, but their values of $Q_{\rm sat}$ are much larger than those considered here. It was concluded that the GW190814 event is likely to be a low-mass black hole rather than a supramassive neutron star. Here we confirm the conclusion reached earlier that hyperonization precludes highly massive hypernuclear stars. The lower panel of Fig. 7 also shows two additional candidates for the mass-gap objects: the GW230529 event where the more massive object has an inferred mass in the range $2.5 \leq M/M_\odot \leq 4.5$ [63] and PSRJ0514-4002E with the mass range of the primary $2.09 \leq M/M_\odot \leq 2.71$ [64], the heavy member in the GW230529 event (light green), and the heavy companion of PSR J0514-4002E (violet). Since the lower limit for GW230529 coincides with errors with the GW190814, our conclusions apply to this object as well. The lower limit on the mass of the companion of PSRJ0514-4002E allows for a hypernuclear neutron star even without rotation.

In addition to the constraints on the mass-radius diagram, the dimensionless tidal deformability Λ inference for the GW170817 offers an additional constraint on the EoS of dense matter. For the nucleonic models adopted here, the deformabilities were computed in Ref. [14] and are shown in Fig. 8. The GW170817 event sets an upper limit on tidal deformability $\Lambda_{1.4} < 800$ for an $1.4M_\odot$ star [61]. The deformability computed for the present models exceeds this limit for $M \leq 1.39M_\odot$ in the case of DDLS70 model, $M \leq 1.34M_\odot$ for DDLS50 model and $M \leq 1.30M_\odot$ for the DDLS30 model, i.e., for current models the tidal deformability of a $1.4M_\odot$ mass star is consistent with the bound above. The hyperonic sequences branch off from the nucleonic ones when the mass is above $M \simeq 1.6M_\odot$ - the upper range of the mass of one of the stars involved in GW170817. Therefore, constraints on hyperonic sequences are the same as for the

nucleonic ones. Nevertheless, we note that hyperonic models are softer than their nucleonic counterparts and consequently their deformabilities are smaller than the nucleonic ones for stars that have central densities above the hyperon onset, i.e. a high enough mass, see e.g. Ref. [76] for more details.

5 Comparison with previous work

We complement now the discussion of our results with a brief comparison of the models used in this work with those that exist in the literature and are available on COMPOSE repository. Our focus is on the general-purpose EoS, i.e., those that cover the density-temperature and electron fraction parameter space. In addition, we will restrict our discussion to those models that include hyperons and at the same time allow for a cold maximum TOV mass above the current observational lower limit $M \gtrsim 2M_\odot$. These restrictions reduce the number of alternatives further.

In general, differences among various models within the hyperonic sector become more pronounced at low temperatures and higher densities, rather than in dilute and hot matter because they arise mainly from the modeling of the interactions. Furthermore, the model uncertainties present in the purely nucleonic sector propagate in the hyperonic sector through the mutual dependence of the baryon octet chemical potentials imposed by baryon conservation and charge neutrality. To give an example, we note that a small magnitude of the symmetry energy of nucleonic matter disfavors hyperons [9]. As mentioned above, the requirement that the maximum mass of a cold hypernuclear star be larger than the observational limit $2M_\odot$, favors nucleonic models with hard EoS and hyperonic interactions that become sufficiently repulsive at high densities. These features have been discussed extensively in the context of the "hyperon puzzle", for reviews see [5,82].

Let us start our discussion with the nucleonic parametrizations that have been used as a basis for extensions to the hypernuclear sector. We list their nuclear characteristics in Table 3. They can be divided into several classes.

1. CDFs with density-dependent couplings. References [8–10,71] developed models based on the DD2 [55] parameterization and their extension to the hypernuclear sector including the full baryon octet; some of the models include also Δ-resonances [10,71]. The hypernuclear models of Refs. [83] based on the same parametrization include Λ hyperons only. The nucleonic DD2 model [55] predicts a moderate value of the slope of the symmetry energy $L_{\rm sym} = 55$ MeV and standard values of the remaining characteristics of nuclear matter. Among our models, the DDLS(50) model thus has a similar value $L_{\rm sym} = 50$ MeV. However, there are stronger variations in the values of $Q_{\rm sat}$, specifically $Q_{\rm sat} = 479.22$ MeV

Table 3 Nuclear characteristics at saturation density of models for which general-purpose EoS for hypernuclear matter are available on CoMPOSE database. Here E_B is the binding energy per particle in symmetrical nuclear matter at saturation density n_{sat} and K is the compressibility. Note that the symmetry energy E_{sym} of models DDLS(30), DDLS(50) and DDLS(70) is fixed at the crossing-density 0.110 fm^{-3} to value $E_{sym} = 27.09$ MeV corresponding to the one predicted by the DDME2 functional. Consequently, the symmetry energy and its slope coefficient L at saturation density are changing in a correlated manner

Model	n_{sat} (fm^{-3})	$-E_B$ (MeV)	K (MeV)	E_{sym} (MeV)	L (MeV)	References
DD2	0.149	16.0	243	31.7	55.0	[55]
DDME2	0.152	16.14	251	32.3	51.3	[77]
DDLS(30)	0.152	16.14	251	30.1	30	[14]
DDLS(50)	0.152	16.14	251	32.2	50	[14]
DDLS(70)	0.152	16.14	251	34.0	70	[14]
QMC	0.156	16.2	292	28.5	54	[78]
CMF	0.150	16.0	300	30.0	88	[79]
SFHo	0.158	16.2	245	31.6	47.1	[80]
FSU2H	0.150	16.28	238	30.2	41.0	[81]

for the DDME2 model [77], $Q_{sat} = 169.15$ MeV for the DD2 model, and $Q_{sat} = 400$ MeV in the present work. All models guarantee that hyperonic stars have masses larger than the two-solar limit; present models allow to vary L_{sym} parameter and explore its influence on various astrophysical scenarios.

2. Quark-meson coupling model. Reference [78] generated tables for these types of models that include a hyperonic component; these are labeled in the CoMPOSE database as SDGTT(QMC-A). As can be seen from Table 3, the slope of the symmetry energy is close to the DDLS(50) model. However, the symmetry energy at saturation is smaller compared DDLS(50) model and other models discussed above, which implies that its value at the crossing density of $n_B = 0.110$ fm^{-3} is likewise smaller than for the rest of the model collec-

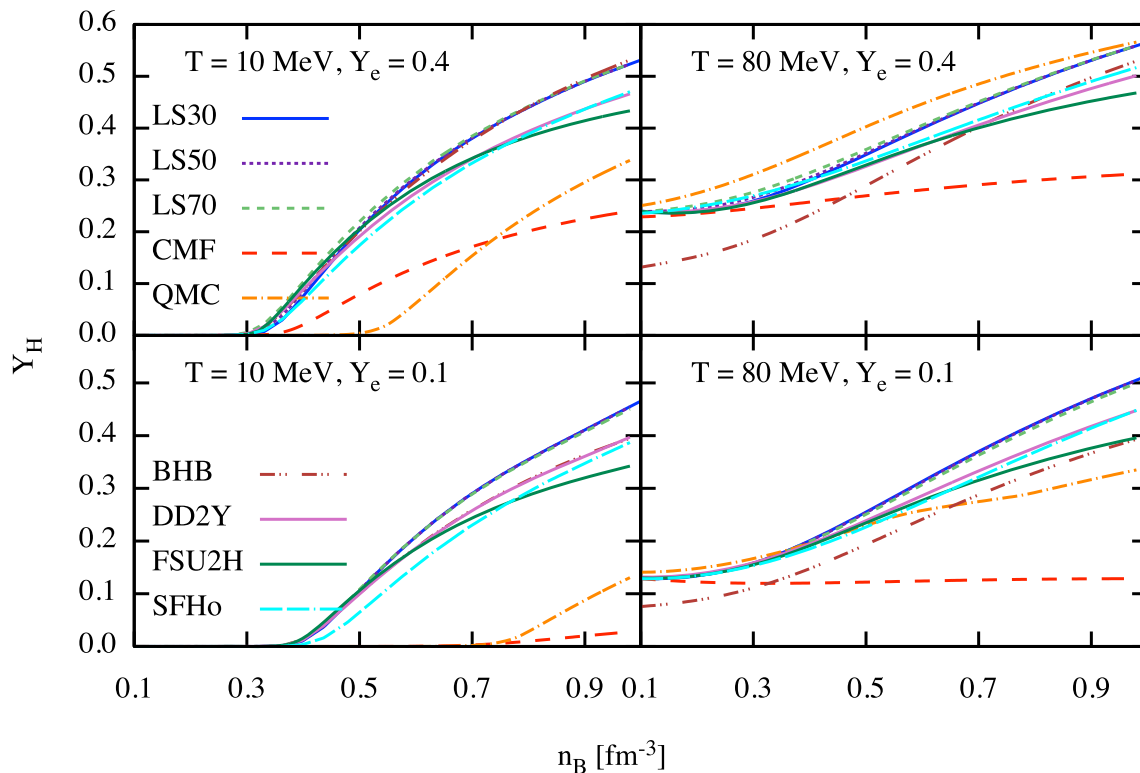**Fig. 9** A comparison of hyperon fraction Y_H as a function of baryon density for various fixed values of temperature T and electron fraction Y_e as predicted by different EoS models. The labelings of various curves are explained in the text

tion. Another notable difference is that the compressibility of nuclear matter is by about 20% larger than in the models used here.

3. Chiral mean-field (CMF) model. This model [labeled in COMPOSE database as DNS(CMF)] is based on a non-linear realization of the sigma model which includes pseudo-scalar mesons as the angular parameters for the chiral transformation [67,79]. This model has large compressibility (which is comparable to the QMC model) and a value of L_{sym} which is by about 25% larger than the value for DDLS(70) model. The model is characterized by a low-value symmetry energy at saturation and its steep increase at higher densities. It appears that the density-dependence of the symmetry energy of the CMF model differs considerably from other models except for the QMC model.

4. Non-linear mean-field models. These models are based on the CDFs with nonlinear meson self-interactions. The FSU2H parametrization was specifically designed for an extension to the hypernuclear sector [81], see also its updated version in Ref. [**?**] labeled in the COMPOSE database as KRT(FSU2H*). The alternative SFHo [80] parametrization was extended to hypernuclear sector in Ref. [9] and is labeled in the database as OMHN(DD2Y). For both models, the nuclear parameters are close to their central values; in particular, the L_{sym} value is close to the DDLS(50) model used in this work.

In Fig. 9 we display the total hyperon fraction $Y_H = \sum_i Y_i$, where the index i sums over the hyperons, as a function of baryon number density for the same temperatures $T = 10$ and 80 MeV and electron fractions $Y_e = 0.1$ and 0.4 as in Figs. 5 and 6. As already seen above, there is only a slight difference in the hyperon content of the three models based on DDLS(30,50,70) parametrization. The value of Y_H is slightly larger for a larger value of L_{sym}. We anticipate that the variations of the slope of the symmetry energy at saturation density has little influence on the hyperonic content of the models which is determined by the physics at higher densities, where the contribution of the $\boldsymbol{\rho}$-meson responsible for variations in L_{sym} is exponentially suppressed, see Eq. (24). Note also that the magnitude of Y_H at low temperatures is dominated by the Λ hyperons independent of the value of the electron fraction.

At low temperatures, our models and the model BHB($\Lambda\phi$) of Ref. [83] predict the largest hyperon fractions which are nearly identical. Slightly smaller hyperon fractions are predicted by the models OMHN(DD2Y) of Ref. [8] based on DD2 parametrization, model KRT(FSU2H*) of Ref. [13] based on FSU2H* parametrization, and model FOP(SFHoY) [9] based on SFHo parametrization (maximally about 15% reduction). This difference does not change with temperature, as it reflects the differences in the hyperonic parametrizations. At high temperatures, the BHB($\Lambda\phi$) model result devi-

ates more strongly from the other models as it contains only Λ hyperons. This underlines the importance of including hyperon species other than the Λ at high temperatures. The density range where Y_H is non-negligible changes with temperature: In the low-temperature regime, it abruptly increases above the threshold density of hyperons, whereas in the high-temperature regime it extends to much lower densities. While all models exhibit these features, the density dependence, and the magnitude of Y_H predicted by the DNS(CMF) [67,79] model and SDGTT(QMC-A) [78] model are markedly different at low temperatures and there are still some qualitative differences at high temperatures. Our brief review in this section highlights the necessity of a more detailed comparison of the predictions of the modern CDF models in the hyperonic sector. Uncovering the origin of the discrepancies among the CDFs remain an interesting task for the future.

6 Conclusions

In this work, we have computed the EoS and composition of finite temperature nucleonic and hypernuclear matter on three-dimensional grids of temperatures, densities, and electron fractions that are required by input tables for simulations of CCSN and BNS mergers. The homogeneous matter was computed down to $0.5n_{sat}$ and the extension to lower densities was done by matching to the low-density HS(DD2) model. The high-density EoS is based on the DDLS family of parametrizations [14] which allow (in general) variations of the slope of the symmetry energy L_{sym} and skewness Q_{sat}; we have chosen to work with $Q_{\text{sat}} = 400$ MeV which guarantees that the values of maximum masses of hypernuclear stars are above the two solar mass lower bound and changed the value of $L_{\text{sym}} = 30$, 50 and 70 MeV. The range of L_{sym} has been chosen to allow for the current uncertainties in this quantity associated with the measurements of neutron skin experiments as well as radii of neutron stars. Thus, our collection of EoS, among other things, allows one to study the effects of varying the symmetry energy in dynamical transients such as supernova explosions and BNS mergers. The six EoS and composition tables that were generated are available on the COMPOSE database.

Data Availability Statement This manuscript has associated data in a data repository. [Authors' comment: The datasets generated during

and/or analysed during the current study are available in the CompOSE repository, https://compose.obspm.fr.]

References

1. CompOSE Core Team, Typel, S., Oertel, M., Klähn, T., Chatterjee, D., Dexheimer, V. et al., Compose reference manual—version 3.01, compstar online supernovæ equations of state,"harmonising the concert of nuclear physics and astrophysics. Eur. Phys. J. A **58**, 221 (2022). https://doi.org/10.1140/epja/s10050-022-00847-y. https://compose.obspm.fr

2. V. Dexheimer, M. Mancini, M. Oertel, C. Providência, L. Tolos, S. Typel, Quick guides for use of the CompOSE data base. Particles **5**, 346–360 (2022). https://doi.org/10.3390/particles5030028. arXiv:2311.04715

3. M. Oertel, M. Hempel, T. Klähn, S. Typel, Equations of state for supernovae and compact stars. Rev. Mod. Phys. **89**, 015007 (2017). https://doi.org/10.1103/RevModPhys.89.015007. arXiv:1610.03361

4. G. Fiorella Burgio, A.F. Fantina, Nuclear equation of state for compact stars and supernovae. Astrophys. Space Sci. Libr. **457**, 255–335 (2018). https://doi.org/10.1007/978-3-319-97616-7_6. arXiv:1804.03020

5. A. Sedrakian, J.J. Li, F. Weber, Heavy baryons in compact stars. Progr. Part. Nucl. Phys. **131**, 104041 (2023). https://doi.org/10.1016/j.ppnp.2023.104041. arXiv:2212.01086

6. G. Colucci, A. Sedrakian, Equation of state of hypernuclear matter: impact of hyperon-scalar-meson couplings. Phys. Rev. C **87**, 055806 (2013). https://doi.org/10.1103/PhysRevC.87.055806. arXiv:1302.6925

7. E.N.E. van Dalen, G. Colucci, A. Sedrakian, Constraining hypernuclear density functional with Λ-hypernuclei and compact stars. Phys. Lett. B **734**, 383–387 (2014). https://doi.org/10.1016/j.physletb.2014.06.002. arXiv:1406.0744

8. M. Marques, M. Oertel, M. Hempel, J. Novak, New temperature dependent hyperonic equation of state: application to rotating neutron star models and I–Q relations. Phys. Rev. C **96**, 045806 (2017). https://doi.org/10.1103/PhysRevC.96.045806. arXiv:1706.02913

9. M. Fortin, M. Oertel, C. Providência, Hyperons in hot dense matter: what do the constraints tell us for equation of state? PASA **35**, e044 (2018). https://doi.org/10.1017/pasa.2018.32. arXiv:1711.09427

10. A.R. Raduta, M. Oertel, A. Sedrakian, Proto-neutron stars with heavy baryons and universal relations. MNRAS **499**, 914–931 (2020). https://doi.org/10.1093/mnras/staa2491. arXiv:2008.00213

11. A. Sedrakian, A. Harutyunyan, Equation of state and composition of proto-neutron stars and merger remnants with hyperons. Universe **7**, 382 (2021). https://doi.org/10.3390/universe7100382. arXiv:2109.01919

12. A. Sedrakian, A. Harutyunyan, Delta-resonances and hyperons in proto-neutron stars and merger remnants. Eur. Phys. J. A **58**, 137 (2022). https://doi.org/10.1140/epja/s10050-022-00792-w. arXiv:2202.12083

13. H. Kochankovski, A. Ramos, L. Tolos, Equation of state for hot hyperonic neutron star matter. Mon. Not. R. Astron. Soc. **517**, 507–517 (2022). https://doi.org/10.1093/mnras/stac2671. arXiv:2206.11266

14. J.-J. Li, A. Sedrakian, New covariant density functionals of nuclear matter for compact star simulations. APJ **957**, 41 (2023). https://doi.org/10.3847/1538-4357/acfa73. arXiv:2308.14457

15. G.A. Lalazissis, T. Nikšić, D. Vretenar, P. Ring, New relativistic mean-field interaction with density-dependent meson-nucleon couplings. Phys. Rev. C **71**, 024312 (2005). https://doi.org/10.1103/PhysRevC.71.024312

16. M. Hempel, J. Schaffner-Bielich, A statistical model for a complete supernova equation of state. Nucl. Phys. A **837**, 210–254 (2010). https://doi.org/10.1016/j.nuclphysa.2010.02.010. arXiv:0911.4073

17. S. Rosswog, The multi-messenger picture of compact binary mergers. Int. J. Mod. Phys. D **24**, 1530012–52 (2015). https://doi.org/10.1142/S0218271815300128. arXiv:1501.02081

18. L. Baiotti, L. Rezzolla, Binary neutron star mergers: a review of Einstein's richest laboratory. Rep. Progr. Phys. **80**, 096901 (2017). https://doi.org/10.1088/1361-6633/aa67bb. arXiv:1607.03540

19. L. Baiotti, Gravitational waves from neutron star mergers and their relation to the nuclear equation of state. Progr. Part. Nucl. Phys. **109**, 103714 (2019). https://doi.org/10.1016/j.ppnp.2019.103714. arXiv:1907.08534

20. S. Blacker, H. Kochankovski, A. Bauswein, A. Ramos, L. Tolos, Thermal behavior as indicator for hyperons in binary neutron star merger remnants. Phys. Rev. D **109**, 043015 (2024). https://doi.org/10.1103/PhysRevD.109.043015. arXiv:2307.03710

21. M. Branchesi et al., Science with the Einstein Telescope: a comparison of different designs. JCAP **07**, 068 (2023). https://doi.org/10.1088/1475-7516/2023/07/068. arXiv:2303.15923

22. S. Khadkikar, A.R. Raduta, M. Oertel, A. Sedrakian, Maximum mass of compact stars from gravitational wave events with finite-temperature equations of state. Phys. Rev. C **103**, 055811 (2021). https://doi.org/10.1103/PhysRevC.103.055811. arXiv:2102.00988

23. M.G. Alford, S.P. Harris, Damping of density oscillations in neutrino-transparent nuclear matter. Phys. Rev. C **100**, 035803 (2019). https://doi.org/10.1103/PhysRevC.100.035803. arXiv:1907.03795

24. M. Alford, A. Harutyunyan, A. Sedrakian, Bulk viscosity of baryonic matter with trapped neutrinos. Phys. Rev. D **100**, 103021 (2019). https://doi.org/10.1103/PhysRevD.100.103021. arXiv:1907.04192

25. M. Alford, A. Harutyunyan, A. Sedrakian, Bulk viscous damping of density oscillations in neutron star mergers. Particles **3**, 500–517 (2020). https://doi.org/10.3390/particles3020034. arXiv:2006.07975

26. M. Alford, A. Harutyunyan, A. Sedrakian, Bulk viscosity from Urca processes: $n\,p\,e\,\mu$ matter in the neutrino-trapped regime. Phys. Rev. D **104**, 103027 (2021). https://doi.org/10.1103/PhysRevD.104.103027. arXiv:2108.07523

27. M.G. Alford, A. Haber, Strangeness-changing rates and hyperonic bulk viscosity in neutron star mergers. Phys. Rev. C **103**, 045810 (2021). https://doi.org/10.1103/PhysRevC.103.045810. arXiv:2009.05181

28. M. Alford, A. Harutyunyan, A. Sedrakian, Bulk viscosity of relativistic npeμ matter in neutron-star mergers. Particles **5**, 361–376 (2022). https://doi.org/10.3390/particles5030029. arXiv:2209.04717

29. E.R. Most, A. Haber, S.P. Harris, Z. Zhang, M.G. Alford, J. Noronha, Emergence of microphysical bulk viscosity in binary neutron star postmerger dynamics. ApJ Lett. **967**, L14 (2024). https://doi.org/10.3847/2041-8213/ad454f

30. T. Celora, I. Hawke, P.C. Hammond, N. Andersson, G.L. Comer, Formulating bulk viscosity for neutron star simulations. Phys. Rev. D **105**, 103016 (2022). https://doi.org/10.1103/PhysRevD.105.103016. arXiv:2202.01576

31. E.R. Most, S.P. Harris, C. Plumberg, M.G. Alford, J. Noronha, J. Noronha-Hostler et al., Projecting the likely importance of weak-interaction-driven bulk viscosity in neutron s tar mergers. MNRAS **509**, 1096–1108 (2022). https://doi.org/10.1093/mnras/stab2793. arXiv:2107.05094

32. M. Prakash, I. Bombaci, M. Prakash, P.J. Ellis, J.M. Lattimer, R. Knorren, Composition and structure of protoneutron stars. Phys. Rep. **280**, 1–77 (1997). https://doi.org/10.1016/S0370-1573(96)00023-3. arXiv:nucl-th/9603042

33. J.A. Pons, S. Reddy, M. Prakash, J.M. Lattimer, J.A. Miralles, Evolution of proto-neutron stars. APJ **513**, 780–804 (1999). https://doi.org/10.1086/306889. arXiv:astro-ph/9807040

34. H.T. Janka, K. Langanke, A. Marek, G. Martínez-Pinedo, B. Müller, Theory of core-collapse supernovae. Phys. Rep. **442**, 38–74 (2007). https://doi.org/10.1016/j.physrep.2007.02.002. arXiv:astro-ph/0612072

35. T. Foglizzo, R. Kazeroni, J. Guilet, F. Masset, M. González, B.K. Krueger et al., The explosion mechanism of core-collapse supernovae: progress in supernova theory and experiments. PASA **32**, e009 (2015). https://doi.org/10.1017/pasa.2015.9. arXiv:1501.01334

36. E.P. O'Connor, S.M. Couch, Exploring fundamentally three-dimensional phenomena in high-fidelity simulations of core-collapse supernovae. APJ **865**, 81 (2018). https://doi.org/10.3847/1538-4357/aadcf7. arXiv:1807.07579

37. A. Burrows, D. Radice, D. Vartanyan, H. Nagakura, M.A. Skinner, J.C. Dolence, The overarching framework of core-collapse supernova explosions as revealed by 3D FORNAX simulations. MNRAS **491**, 2715–2735 (2020). https://doi.org/10.1093/mnras/stz3223. arXiv:1909.04152

38. A. Pascal, J. Novak, M. Oertel, Proto-neutron star evolution with improved charged-current neutrino-nucleon interactions. MNRAS **511**, 356–370 (2022). https://doi.org/10.1093/mnras/stac016. arXiv:2201.01955

39. A. Mezzacappa, *Toward realistic models of core collapse supernovae: a brief review*, in *The Predictive Power of Computational Astrophysics as a Discover Tool, vol. 362*, ed. by D. Bisikalo, D. Wiebe, C. Boily (2023), pp. 215–227. (2023). arXiv:2205.13438

40. K. Sumiyoshi, S. Yamada, H. Suzuki, Dynamics and neutrino signal of black hole formation in nonrotating failed supernovae. I. Equation of state dependence. APJ **667**, 382–394 (2007). https://doi.org/10.1086/520876. arXiv:0706.3762

41. T. Fischer, S.C. Whitehouse, A. Mezzacappa, F.K. Thielemann, M. Liebendörfer, The neutrino signal from protoneutron star accretion and black hole formation. A&A **499**, 1–15 (2009). https://doi.org/10.1051/0004-6361/200811055. arXiv:0809.5129

42. E. O'Connor, C.D. Ott, Black hole formation in failing core-collapse supernovae. APJ **730**, 70 (2011). https://doi.org/10.1088/0004-637X/730/2/70. arXiv:1010.5550

43. A. da Silva Schneider, E. O'Connor, E. Granqvist, A. Betranhandy, S.M. Couch, Equation of state and progenitor dependence of stellar-mass black hole formation. APJ **894**, 4 (2020). https://doi.org/10.3847/1538-4357/ab8308. arXiv:2001.10434

44. R. Bollig, H.T. Janka, A. Lohs, G. Martinez-Pinedo, C.J. Horowitz, T. Melson, Muon creation in supernova matter facilitates neutrino-driven explosions. Phys. Rev. Lett. **119**, 242702 (2017). https://doi.org/10.1103/PhysRevLett.119.242702. arXiv:1706.04630

45. D. Chatterjee, T. Elghozi, J. Novak, M. Oertel, Consistent neutron star models with magnetic-field-dependent equations of state. MNRAS **447**, 3785–3796 (2015). https://doi.org/10.1093/mnras/stu2706. arXiv:1410.6332

46. V.B. Thapa, M. Sinha, J.J. Li, A. Sedrakian, Equation of state of strongly magnetized matter with hyperons and Δ-resonances. Particles **3**, 660–675 (2020). https://doi.org/10.3390/particles3040043

47. J. Peterson, P. Costa, R. Kumar, V. Dexheimer, R. Negreiros, C. Providência, Temperature and strong magnetic field effects in dense matter. Phys. Rev. D **108**, 063011 (2023). https://doi.org/10.1103/PhysRevD.108.063011. arXiv:2304.02454

48. M. Stein, J. Maruhn, A. Sedrakian, P.G. Reinhard, Carbon-oxygen–neon mass nuclei in superstrong magnetic fields. Phys. Rev. C **94**, 035802 (2016). https://doi.org/10.1103/PhysRevC.94.035802. arXiv:1607.04398

49. L. Scurto, H. Pais, F. Gulminelli, Strong magnetic fields and pasta phases reexamined. Phys. Rev. C **107**, 045806 (2023). https://doi.org/10.1103/PhysRevC.107.045806. arXiv:2212.09355

50. V. Parmar, H.C. Das, M.K. Sharma, S.K. Patra, Magnetized neutron star crust within effective relativistic mean-field model. Phys. Rev. D **107**, 043022 (2023). https://doi.org/10.1103/PhysRevD.107.043022. arXiv:2211.07339

51. V.N. Kondratyev, Properties and composition of magnetized nuclei. Particles **3**, 272–277 (2020). https://doi.org/10.3390/particles3020021

52. S. Typel, Relativistic mean-field models with different parametrizations of density dependent couplings. Particles **1**, 2 (2018). https://doi.org/10.3390/particles1010002

53. J.M. Lattimer, Constraints on nuclear symmetry energy parameters. Particles **6**, 30–56 (2023). https://doi.org/10.3390/particles6010003. arXiv:2301.03666

54. S. Typel, H.H. Wolter, Relativistic mean field calculations with density-dependent meson–nucleon coupling. Nucl. Phys. A **656**, 331–364 (1999). https://doi.org/10.1016/S0375-9474(99)00310-3

55. S. Typel, G. Röpke, T. Klähn, D. Blaschke, H.H. Wolter, Composition and thermodynamics of nuclear matter with light clusters. Phys. Rev. C **81**, 015803 (2010). https://doi.org/10.1103/PhysRevC.81.015803. arXiv:0908.2344

56. M. Oertel, F. Gulminelli, C. Providência, A.R. Raduta, Hyperons in neutron stars and supernova cores. Eur. Phys. J. A **52**, 50 (2016). https://doi.org/10.1140/epja/i2016-16050-1. arXiv:1601.00435

57. T.E. Riley, A.L. Watts, S. Bogdanov, P.S. Ray, R.M. Ludlam, S. Guillot et al., A NICER view of PSR J0030+0451: millisecond pulsar parameter estimation. APJ **887**, L21 (2019). https://doi.org/10.3847/2041-8213/ab481c. arXiv:1912.05702

58. M.C. Miller, F.K. Lamb, A.J. Dittmann, S. Bogdanov, Z. Arzoumanian, K.C. Gendreau et al., PSR J0030+0451 mass and radius from NICER data and implications for the properties of neutron star matter. APJ **887**, L24 (2019). https://doi.org/10.3847/2041-8213/ab50c5. arXiv:1912.05705

59. T.E. Riley, A.L. Watts, P.S. Ray, S. Bogdanov, S. Guillot, S.M. Morsink et al., A NICER view of the massive pulsar PSR J0740+6620 informed by radio timing and XMM-Newton spectroscopy. APJ **918**, L27 (2021). https://doi.org/10.3847/2041-8213/ac0a81. arXiv:2105.06980

60. M.C. Miller, F.K. Lamb, A.J. Dittmann, S. Bogdanov, Z. Arzoumanian, K.C. Gendreau et al., The Radius of PSR J0740+6620 from NICER and XMM-Newton data. APJ **918**, L28 (2021). https://doi.org/10.3847/2041-8213/ac089b. arXiv:2105.06979

61. B.P. Abbott, R. Abbott, T.D. Abbott, F. Acernese, K. Ackley, C. Adams et al., GW170817: observation of gravitational waves from a binary neutron star inspiral. Phys. Rev. Lett **119**,

161101 (2017). https://doi.org/10.1103/PhysRevLett.119.161101. arXiv:1710.05832

62. R. Abbott, T.D. Abbott, S. Abraham, F. Acernese, K. Ackley, C. Adams et al., GW190814: gravitational waves from the coalescence of a 23 solar mass black hole with a 2.6 solar mass compact object. APJ **896**, L44 (2020). https://doi.org/10.3847/2041-8213/ab960f. arXiv:2006.12611

63. Ligo-Virgo-Kagra Collaboration, Observation of gravitational waves from the coalescence of a 2.5–4.5 $M_\odot$ compact object and a neutron star. preprint arXiv

64. E.D. Barr et al., A pulsar in a binary with a compact object in the mass gap between neutron stars and black holes. Science **383**, 275–279 (2024). https://doi.org/10.1126/science.adg3005. arXiv:2401.09872

65. J.R. Oppenheimer, G.M. Volkoff, On massive neutron cores. Phys. Rev. **55**, 374–381 (1939). https://doi.org/10.1103/PhysRev.55.374

66. N. Stergioulas, J.L. Friedman, Comparing models of rapidly rotating relativistic stars constructed by two numerical methods. APJ **444**, 306 (1995). https://doi.org/10.1086/175605. arXiv:astro-ph/9411032

67. T. Schürhoff, S. Schramm, V. Dexheimer, Neutron stars with small radii-the role of Δ resonances. APJ **724**, L74–L77 (2010). https://doi.org/10.1088/2041-8205/724/1/L74. arXiv:1008.0957

68. A. Drago, A. Lavagno, G. Pagliara, D. Pigato, Early appearance of Δ isobars in neutron stars. Phys. Rev. C **90**, 065809 (2014). https://doi.org/10.1103/PhysRevC.90.065809

69. B.-J. Cai, F.J. Fattoyev, B.-A. Li, W.G. Newton, Critical density and impact of Δ (1232) resonance formation in neutron stars. Phys. Rev. C **92**, 015802 (2015). https://doi.org/10.1103/PhysRevC.92.015802. arXiv:1501.01680

70. G. Malfatti, M.G. Orsaria, I.F. Ranea-Sandoval, G.A. Contrera, F. Weber, Delta baryons and diquark formation in the cores of neutron stars. Phys. Rev. D **102**, 063008 (2020). https://doi.org/10.1103/PhysRevD.102.063008. arXiv:2008.06459

71. A.R. Raduta, Equations of state for hot neutron stars-II. The role of exotic particle degrees of freedom. Eur. Phys. J. A **58**, 115 (2022). https://doi.org/10.1140/epja/s10050-022-00772-0. arXiv:2205.03177

72. A. Sedrakian, F. Weber, J.J. Li, Confronting GW190814 with hyperonization in dense matter and hypernuclear compact stars. Phys. Rev. D **102**, 041301 (2020). https://doi.org/10.1103/PhysRevD.102.041301. arXiv:2007.09683

73. J.J. Li, A. Sedrakian, F. Weber, Rapidly rotating Δ-resonance-admixed hypernuclear compact stars. Phys. Lett. B **810**, 135812 (2020). https://doi.org/10.1016/j.physletb.2020.135812

74. V. Dexheimer, R.O. Gomes, T. Klähn, S. Han, M. Salinas, GW190814 as a massive rapidly rotating neutron star with exotic degrees of freedom. Phys. Rev. C **103**, 025808 (2021). https://doi.org/10.1103/PhysRevC.103.025808. arXiv:2007.08493

75. H.R. Fu, J.J. Li, A. Sedrakian, F. Weber, Massive relativistic compact stars from SU(3) symmetric quark models. Phys. Lett. B **834**, 137470 (2022). https://doi.org/10.1016/j.physletb.2022.137470. arXiv:2209.05699

76. J.J. Li, A. Sedrakian, Implications from GW170817 for Δ-isobar Admixed hypernuclear compact stars. APJ **874**, L22 (2019). https://doi.org/10.3847/2041-8213/ab1090. arXiv:1904.02006

77. J.J. Li, A. Sedrakian, Constraining compact star properties with nuclear saturation parameters. Phys. Rev. C **100**, 015809 (2019). https://doi.org/10.1103/PhysRevC.100.015809

78. J.R. Stone, V. Dexheimer, P.A.M. Guichon, A.W. Thomas, S. Typel, Equation of state of hot dense hyperonic matter in the quark-meson-coupling (QMC-A) model. MNRAS **502**, 3476–3490 (2021). https://doi.org/10.1093/mnras/staa4006. arXiv:1906.11100

79. V. Dexheimer, R. Negreiros, S. Schramm, Reconciling nuclear and astrophysical constraints. Phys. Rev. C **92**, 012801 (2015). https://doi.org/10.1103/PhysRevC.92.012801

80. A.W. Steiner, M. Hempel, T. Fischer, Core-collapse supernova equations of state based on neutron star observations. APJ **774**, 17 (2013). https://doi.org/10.1088/0004-637X/774/1/17. arXiv:1207.2184

81. L. Tolos, M. Centelles, A. Ramos, Equationn of state for nucleonic and hyperonic neutron stars with mass and radius constraints. APJ **834**, 3 (2017). https://doi.org/10.3847/1538-4357/834/1/3. arXiv:1610.00919

82. D. Chatterjee, I. Vidaña, Do hyperons exist in the interior of neutron stars? Eur. Phys. J. A **52**, 29 (2016). https://doi.org/10.1140/epja/i2016-16029-x. arXiv:1510.06306

83. S. Banik, M. Hempel, D. Bandyopadhyay, New hyperon equations of state for supernovae and neutron stars in density-dependent hadron field theory. ApJS **214**, 22 (2014). https://doi.org/10.1088/0067-0049/214/2/22. arXiv:1404.6173